Breakdown of Hund's third rule in amorphous Co-W nanoparticles and crystalline Co_3W alloys

A. I. Figueroa,* F. Bartolomé, J. Bartolomé, and L. M. García
Instituto de Ciencia de Materiales de Aragón (ICMA), CSIC - Universidad de Zaragoza, Departamento de Física de la Materia Condensada, E-50009 Zaragoza, Spain

F. Petroff and C. Deranlot
Unité Mixte de Physique CNRS/Thales, F-91767 Palaiseau Cedex, France and Université Paris-Sud, F-91405 Orsay Cedex, France

F. Wilhelm and A. Rogalev
European Synchrotron Radiation Facility (ESRF), F-38043 Grenoble, France
(Received 26 May 2012; revised manuscript received 20 July 2012; published 20 August 2012)

We present x-ray absorption near edge structure (XANES) and x-ray magnetic circular dichroism (XMCD) measurements performed at the Co K and W $L_{2,3}$ edges, on amorphous Co-W alloy nanoparticles, and a comparison with those on a bulk Co_3W alloy. A strong hybridization between the $4p$ and $3d$ orbitals in Co and the $5d$ band in W are observed, resulting in an induced magnetic moment in the W atoms. The orbital to spin moment ratio in W of all these Co-W systems is positive, suggesting a parallel orientation of the two moments. This is opposite to the expected antiparallel coupling for atoms with a less-than-half-filled $5d$ band, according to Hund's third rule. These findings are supported by calculations of the electronic density of states projected at the Co $3d$ and W $5d$ orbitals, as well as XANES spectra and XMCD signals at the Co K and W $L_{2,3}$ edges in a Co_3W system.

DOI: 10.1103/PhysRevB.86.064428 PACS number(s): 75.75.Fk, 75.50.Kj, 71.20.Be, 78.70.Dm

I. INTRODUCTION

Magnetic nanoparticles (NPs) have recently been the focus of much research because of their scientific and technological interest in diverse fields.[1,2] Extensive magnetic characterization of these particles has been carried out with the element-specific x-ray magnetic circular dichroism (XMCD) technique. It arises as an effective method to selectively study the magnetic properties of the particles, giving access to both contributions to the total magnetic moment, the orbital m_L and spin moment m_S. It is then an important tool to study the magnetic anisotropy of these nanoparticles systems, e.g., to evaluate the contribution of the orbital moment to this anisotropy as a result of the symmetry breaking at the particle surface.[1,3–8]

However, not all magnetic nanoparticles have their anisotropy originated on surface effects. In particular, among the specific group of magnetic nanoparticles with amorphous structure, the amorphous Co-W alloy NPs constitute a paradigmatic example, where their anisotropy is not due to surface effects but results from the structural short range order (SRO) detected in the particles.[9] They consist of a self-organized array of Co-W alloy particles, uniformly dispersed in an alumina matrix. Their magnetic properties are those of noninteracting superparamagnetic particles with random anisotropy axes and an average moment per particle proportional to the particle volume, governed by the Co/W ratio present in the alloy. The morphological, structural, and magnetic properties of these particles have been extensively described in Ref. 9. Co-W hybridization and electronic transfer from W $5d$ to Co orbitals are also determined by analysis of x-ray absorption near edge structure (XANES) measurements at the Co K and W L_3 edges. The electronic transfer from W $5d$ toward Co $4p$ bands, and the delocalization of the Co $3d$ empty states are qualitatively described as a function of the Co/W ratio in these Co-W NPs samples.[9]

The effects of similar $3d-5d$ hybridization, in particular on $5d$ induced magnetic moments, have been previously studied both experimentally and theoretically in Fe/W multilayers[10] and bulk $Co_{100-x}Ir_x$ alloys,[11] to cite some examples of metallic systems. A remarkable finding in these two systems is the observation of a breakdown of Hund's third rule of the induced orbital and spin magnetic moments in the $5d$ metals. This rule states how spin and orbital total moments in a single atom should be aligned, being parallel for an atom with a more than half-filled shell, and antiparallel for a less than half-filled shell.[12] In spite of its phenomenological character and of being defined for single isolated atoms, atoms in solids have been proven to ubiquitously follow this rule, too.

However, the two cases mentioned above are part of the few examples where this rule is not completely fulfilled.[10,11,13–15] In the Fe/W multilayers, the total spin and orbital magnetic moments of the $5d$ W shell couple in parallel (notice that W is a less than half-filled $5d$ band metal), and for Ir in bulk Co-Ir alloys they are antiparallel aligned (Ir is a more than half-filled $5d$ band metal), being, in both cases, contrary to the predictions of Hund's third rule.[10,11] All these experimental findings have been possible thanks to the highly sensitive XMCD technique, which, as stated above, allows us to perform element specific magnetometry, as well as to separate the contribution of the orbital and spin moments to the total magnetic moment and their relative orientation, by applying the magneto-optical sum rules.[16,17]

The structural disorder in transition metal alloys has also been demonstrated to influence their electronic configuration.[14] In fact, for amorphous Fe-Zr and Co-Zr alloy films, the induced spin and orbital moments detected in Zr (a less-than half filled $4d$ element) are found to be parallel aligned, thus breaking down Hund's third rule. However, for similar crystalline compounds Fe-Zr-Pt and Co-Zr-Pt, the

induced orbital and spin moments in Zr are found to fulfill this rule.

Under this scheme, the amorphous Co-W alloy NPs arise as an attractive system to investigate the hybridization between Co orbitals and the 5*d* band of W, and its consequence on the induced magnetic moments in W. XANES and XMCD are the best techniques to study the electronic transfer between Co and W, and to examine the compliance or breakdown of Hund's third rule in the W atoms in Co-W systems. This paper is then dedicated to delving into those hybridization effects, both experimentally, by XANES and XMCD measurements at the Co K and W $L_{2,3}$ edges, and theoretically, by simulations of the XANES and XMCD signals at both edges in the amorphous Co-W alloy NPs system. A polycrystalline bulk Co_3W alloy is also included in the present study, so that, by comparison to the amorphous NPs, the influence of the structural disorder is evaluated.

The paper is organized as follows. In Sec. II we describe the preparation of the samples studied along with their morphology and structural properties. The experimental results are presented in Sec. III and the calculations in Sec. IV. Finally, we summarize and conclude our paper in Sec. V.

II. SAMPLES PREPARATION, MORPHOLOGY AND STRUCTURE

The Co-W NPs samples were prepared by sequential sputtering deposition of Al_2O_3, Co and W on a Si substrate, following the same procedure as is described in previous works on metal capped Co nanoparticles.[4,9] These samples follow the formula $Al_2O_3/(Al_2O_3/Co/W)_N/Al_2O_3$, with N being the number that the sequence is repeated in order to obtain a multilayer system. Two series of samples were studied: *a*, samples with a fixed nominal thickness of deposited Co, $t_{Co} = 0.7$ nm, and different amounts of W given by $t_W = 0.6$, 1.5, and 4.5 nm; *b*, samples with constant $t_W = 1.5$ nm and varying $t_{Co} = 0.7$ and 1.0 nm. In most cases $N = 25$, except for the sample with $t_{Co} = 1.0$ nm and $t_W = 1.5$ nm, for which $N = 20$.

These samples form a system of self-organized and uniformly dispersed amorphous Co-W alloy NPs. Their size and composition are controlled by varying the amount of Co or W in the system. The amorphous nature of the particles has been proven by high resolution transmission electron microscopy (HRTEM) and extended x-ray absorption fine structure (EXAFS). The composition of the $Co_{1-x}W_x$ alloy in the NPs samples used in the present study varies between 14.1 and 18.8 % at.W, as listed in Table I. Both HRTEM and EXAFS show evidences of metallic W in all samples; i.e., when the amount of W in the sample increases and the Co-W alloy saturates, W grows as a crystal and fills the interparticle spaces.

A bulk Co_3W alloy has been used in the present study as a reference sample. It has been synthesized by melting the pure metallic precursors in an induction furnace under Ar atmosphere. The encapsulated sample was thermally treated for seven days at a temperature of 1300 K in a muffle furnace. After the annealing, the sample was quenched by immersing the quartz tube in room temperature water.

The chemical composition of the bulk Co_3W alloy was confirmed by means of energy-dispersive x-ray spectroscopy (EDX) performed by an Oxford Instruments INCA 300 X-Sight as part of a JEOL JSM 6400 scanning electron microscope (SEM). The crystalline structure of the alloy was determined by x-ray powder diffraction (XRD) measurements performed at room temperature using a rotating anode D-Max Rigaku diffractometer. XRD data were collected in a range $20^\circ < 2\theta < 80^\circ$ using Cu K_α radiation, and are shown in Fig. 1(a). The Co_3W alloy is an *hcp* phase with spatial group $P6_3mc$. A profile matching (PM) routine was run on this data using FULLPROF suite code.[18] The position of the diffraction peaks in the XRD profile are well matched with this routine using the Co_3W crystallographic information taken from the ICSD database[19] as initial parameters [see Fig. 1(a)]. The lattice parameters obtained from the PM for the bulk Co_3W alloy were $a = b = 5.144$Å and $c = 4.141$ Å, very close to those of the Co_3W listed in the ICSD. However, the structure in the bulk Co_3W sample is found to be rather disordered, which is evident from the broad and less intense diffraction peaks observed, compared to regular highly crystalline materials, and from the mismatch of the peaks width in the PM results. Thus, a complete Rietveld analysis on this dataset was not possible. There are a very few diffraction peaks not identified by the PM routine that may be assigned to the Co_7W_6 phase; such a phase has also been observed in the SEM and EDX study, but it has been estimated to be less than 2% in the sample.

The local structure of the Co-W alloy NPs and the bulk Co_3W alloy has been examined by EXAFS measurements at the Co K (7709 eV) and W L_3 (10207 eV) edges using a double-crystal Si(111) monocromator in the BM29 beamline at the European Synchrotron Radiation Facility (ESRF). Measurements were performed at 300 K in fluorescence detection mode with a 13-element Ge solid state detector with digital signal processing for fluorescence x-ray absorption (XAS), high energy resolution, and high count rate. The R-space EXAFS data at the Co K edge for the bulk Co_3W alloy and for the Co-W NPs sample with $t_{Co} = 0.7$ nm and $t_W = 1.5$ nm are shown in Fig. 1(b). The fitting procedure of these EXAFS data has been previously described in Ref. 9. In fact,

TABLE I. Structural parameters obtained from the EXAFS fits for the Co-W alloy NPs and the bulk Co_3W alloy. Composition in the $Co_{1-x}W_x$ alloy (x, all in % at. W), Co-Co, Co-W, and total coordination numbers (N_{Co-Co}, N_{Co-W}, and N_T, respectively), and interatomic distances (R, all in Å) for each path used in the fitting model.

	Co-W NPs			Bulk
t_{Co}(nm)	1.0	0.7	0.7	
t_W(nm)	1.5	0.6	1.5	Co_3W
x in $Co_{1-x}W_x$	14.1(4)[a]	18.2(4)[a]	18.8(4)[a]	25(1)
R_{Co-Co}	2.32(1)[a]	2.33(2)[a]	2.37(4)[a]	2.02(2)
R_{Co-Co}	2.48(1)[a]	2.46(2)[a]	2.51(5)[a]	2.52(2)
R_{Co-W}	2.21(2)[a]	2.19(2)[a]	2.14(9)[a]	1.90(5)
R_{Co-W}	2.40(2)[a]	2.61(2)[a]	2.63(9)[a]	2.57(5)
R_{Co-Co}	2.82(2)[a]	2.61(2)[a]	2.71(8)[a]	3.19(2)
N_{Co-Co}	8.0(6)[a]	7.4(3)[a]	4.9(8)[a]	8
N_{Co-W}	4.0(6)[a]	4.1(3)[a]	4.5(8)[a]	4
N_T	12.0(6)[a]	11.5(3)[a]	9.4(8)[a]	12

[a]Reference 9.

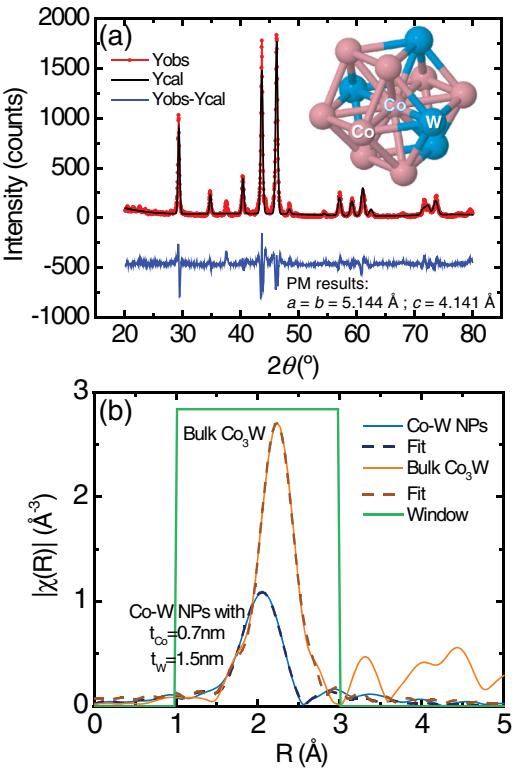

FIG. 1. (Color online) (a) XRD data and PM results for the bulk Co_3W alloy, along with an illustration of the structure of a Co first coordination shell. The lattice parameters obtained from the PM are $a = b = 5.144$ Å and $c = 4.141$ Å. (b) Fourier transformed EXAFS signal at the Co K edge for the bulk Co_3W alloy and comparison with that of a Co-W alloy NPs sample. Dashed lines: best fit of the first Co coordination shell for each sample.

the Co local environment in the Co-W alloy NPs can be seen as an altered Co_3W structure, in which the Co-Co coordination, N_{Co-Co}, and Co-W coordination, N_{Co-W}, vary according to the Co/W ratio in the alloy. An illustration of the Co first coordination shell in the crystal structure of the Co_3W alloy is shown in the inset of Fig. 1(a). In this structure, the central Co is surrounded by a total of 12 atoms ($N_T = 12$, typical in *hcp* structures), from which eight are other Co atoms ($N_{Co-Co} = 8$) and the remaining four are W atoms ($N_{Co-W} = 4$). In the Co-W alloy NPs, N_{Co-Co} is reduced from 8 to values as low as 4.9 and N_{Co-W} increases from 4 to 4.5 as the amount of W in the sample increases. These results are given in Table I. SRO in these samples is evident since N_T still resembles that of the Co_3W crystal. The interatomic distances R in the Co first coordination shell for the Co-W NPs and the bulk Co_3W alloy samples obtained from EXAFS are also listed in Table I. The complete morphological, structural, and magnetic study of these Co-W NPs samples can be found in Ref. 9.

III. XANES AND XMCD MEASUREMENTS

A. Experimental details

XANES and XMCD measurements at the Co K (7709 eV), W L_3 (10207 eV) and W L_2 (11544 eV) edges on the Co-W NPs samples and the bulk Co_3W alloy were performed at the ESRF ID12 beamline. Spectra for Al_2O_3-capped Co NPs and on a W metallic foil for reference, were also recorded, at the Co K and W $L_{2,3}$ edges, respectively. The APPLE-II undulator and a double-Si-(111)-crystal monocromator were used to collect the spectra at the respective energies. XANES spectra were recorded by a fluorescence detector in backscattering geometry. XMCD signal was obtained by applying a magnetic field of 10 and 50 kOe for the Co-W NPs and the Co_3W alloy, respectively, normal to the sample plane and along the x-ray beam direction. Measurements were performed at 7 and 10 K for the Co-W NPs and the Co_3W alloy, respectively. This field and temperature were chosen according to the magnetic properties of the Co-W NPs, so that the system was reaching its magnetic saturation under these conditions.[9] XMCD was obtained by differences of XANES spectra measured with opposite helicities of the light at a fixed magnetic field value, orienting the field in two inverse directions. Polarization of the circular light was over 90% at the Co K edge and 94% at the W $L_{2,3}$ edges. Due to the low XMCD signal in W, several spectra were taken for each sample, being 16 spectra in average for each direction of the field. Due to experimental difficulties, the Co-W NPs sample with $t_{Co} = 0.7$ nm and $t_W = 4.5$ nm was not measured at the W $L_{2,3}$ edges.

The absorption spectra and XMCD for the bulk Co_3W alloy were corrected for self-absorption effects after their normalization of the absorption jump to unity. These corrections take into account that the sample is infinitely thick, and uses its chemical composition and density, along with some geometrical parameters of the measurement setup such as the angle of incidence of the x-ray beam and the solid angle of the detector, to estimate the effect of self-absorption from the known energy dependence of the absorption coefficient of the sample. Details of the correction procedure can be found in Ref. 20 and references therein.

B. Co K edge results

XANES and XMCD at the Co K edge probe the $4p$ empty states of the Co atom in the sample. Analysis of the XANES spectra recorded at this edge on these Co-W alloy NPs samples has been previously reported by us.[9] Evidences of Co $4p-3d$ and Co $3d-$W $5d$ hybridization in the Co-W system and electronic transfer from W $5d$ to Co orbitals were then observed. These findings were obtained not only from the observed changes of the Co K edge XANES on the Co-W alloy NPs with respect to that of metallic Co, but also from the reduction of the magnetic moments of the Co atoms obtained in the Co-W alloy NPs by W inclusion in the alloy, as proven by analysis of the XMCD signals at the Co $L_{2,3}$ edges.[9]

The detection of a nonzero XMCD signal at the Co K edge on all samples, shown in Fig. 2, reflects the magnetic polarization of the $4p$ band in Co atoms. In Fig. 2 we compare the XMCD spectra for all studied samples, normalized to the energy jump of the absorption edge: the Al_2O_3 capped Co NPs [Fig. 2(a)], the a and b samples series [Figs. 2(b) and 2(c), respectively], and the bulk Co_3W alloy [Fig. 2(d)]. The origin of the energy scale has been chosen at the inflection point of the absorption edge. The XMCD signal in the case of the Al_2O_3 capped Co NPs [Fig. 2(a)] emerges by interatomic exchange interaction between the $4p$ band of the absorbing Co and the $3d$ bands of the neighboring Co atoms. This results from

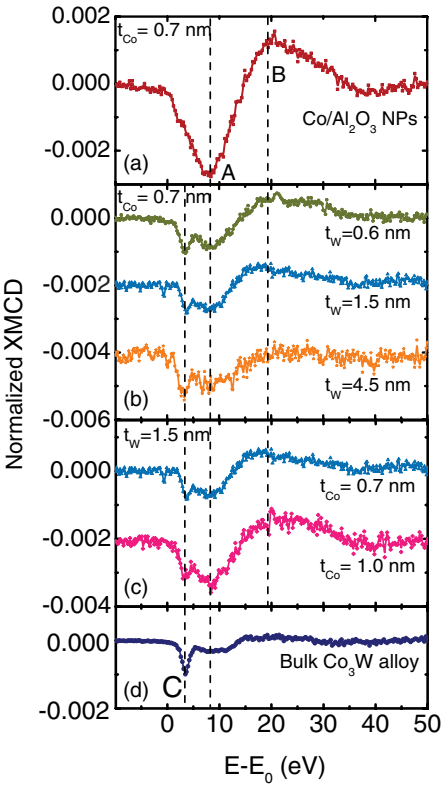

FIG. 2. (Color online) XMCD spectra at the Co K edge for (a) Al_2O_3 capped Co NPs, (b) Co-W NPs a sample series, (c) Co-W NPs b sample series, and (d) bulk Co_3W alloy.

the allowed symmetry operations at the Co site in this cubic structure, so that the $4p-3d$ bands mixing is only possible via the neighboring Co atoms.[21] In the Co-W alloys [Figs. 2(b) to 2(d)], with a hexagonal local structure, this signal originates at the intraatomic exchange interaction between the $4p$ and $3d$ bands in Co. The sign of the XMCD signal in all cases is the same as in Ref. 22, indicating an antiferromagnetic coupling between $4p$ and $3d$ levels in Co.

Visible differences are observed in the Co K edge XMCD spectra of the Co-W NPs with respect to that of Al_2O_3 capped [see Fig. 2(a)]; however, they are very similar to that of the Co_3W alloy [Fig. 2(d)]. The dichroic signal in the Al_2O_3 capped Co NPs consists of a negative one-peak structure between 5 and 10 eV above the edge [marked in Fig. 2(a) as peak A], followed by a positive large bump between 10 eV and 30 eV [denoted in Fig. 2(a) as peak B], similar to what is observed in metallic Co[21] and other metal capped Co NPs.[4] Instead, in our Co-W NPs [Figs. 2(b) and 2(c)] and in the Co_3W alloy [Fig. 2(d)] the broad negative peak A is split, giving rise to a double-peak structure formed by a trace of peak A and an additional negative peak, tagged as C in Fig. 2(d). This peak C is more pronounced in the XMCD signal of the bulk Co_3W alloy. A similar shape of Co K edge XMCD signal has been observed by Rueff *et al.*[21] in $LaCo_5$ alloys, where they discussed the effect of the rare earth on the Co K XMCD signal shape. They ascribe this extra feature in the negative peak to a contribution of the La d empty states. Then, we may conjecture that this splitting in the Co-W systems is due to the W $5d$ states in the Co-W alloy.

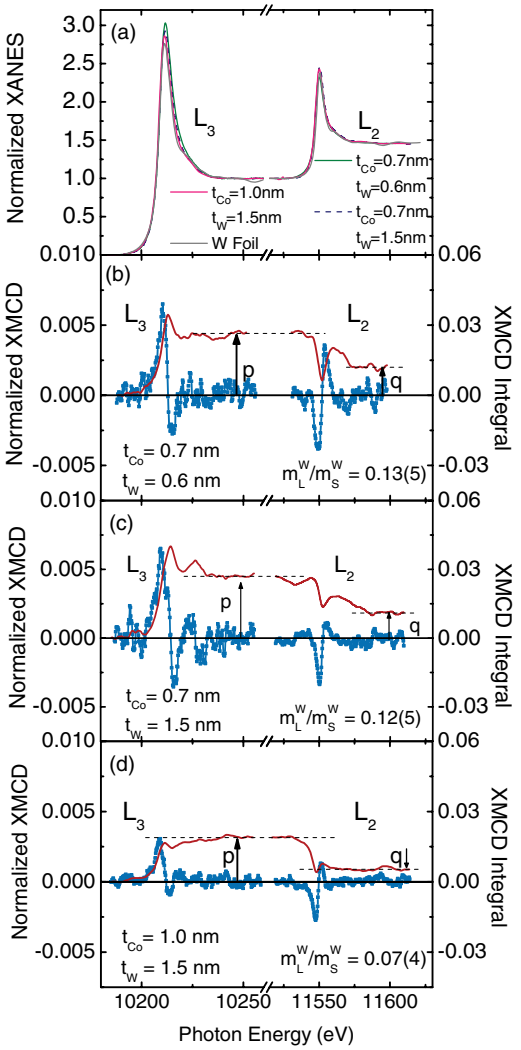

FIG. 3. (Color online) (a) XANES spectra at the W $L_{2,3}$ for the Co-W NPs, and for a W reference foil. (b) to (d) show normalized XMCD signal and XMCD integral for each Co-W alloy NPs sample at the W $L_{2,3}$ measured at $H = 10$ kOe. Arrows indicate the energy at which p and q integrals were determined.

C. W $L_{2,3}$ edges results

XANES spectra recorded at the W $L_{2,3}$ were normalized as L_3/L_2 to 2.19/1, according to Ref. 23. Spectra measured for the Co-W NPs are shown in Fig. 3(a), along with the one for a metallic W foil. XANES of the bulk Co_3W alloy is plotted in Fig. 4(a). Changes in the absorption white line at W $L_{2,3}$ edges for the Co-W NPs are observed and reflect variation of the available states of $5d$ character. Specifically, L_3 absorption edge appears for transitions from $2p$ to both $5d_{3/2}$ and $5d_{5/2}$, while L_2 reveals only transitions from $2p$ to $5d_{3/2}$ band. A qualitative analysis of this variation was reported by us in Ref. 9. We observed that an increase in the Co/W ratio in the Co-W NPs samples gave rise to an increase in the number of W $5d$ empty states, n_h^W; i.e., there is an electron transfer from W toward Co. The change in n_h^W for each sample may be quantified by analysis of the W $L_{2,3}$ XANES spectra. The integral of the white line at the $L_{2,3}$ edges of each sample, r_{Co-W}, and that for W foil, $r_{W,foil}$, are defined

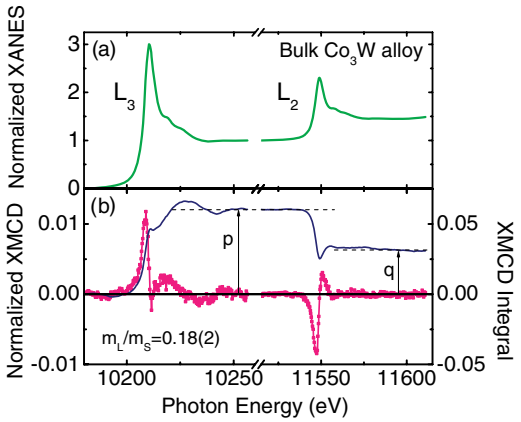

FIG. 4. (Color online) (a) XANES spectra and (b) XMCD signal and XMCD integral at the W $L_{2,3}$ for the Co_3W alloy measured at $H = 50$ kOe and $T = 10$ K. Arrows indicate the energy at which p and q integrals were determined.

as the sum of the individual L_2 and L_3 integrals, I_{L2} and I_{L3}, respectively, calculated by first subtracting the continuum from each XANES. The continuum is artificially represented by a double-step function. This double-step approach is extensively used for the $3d$ metals, and its accuracy in the case of W has been previously estimated to be about 94%, given its relative large white line intensity.[10] Then, assuming that for metallic W $n_h^{\mathrm{W,foil}} = 5.7$ holes,[10] we estimate a scaling factor $C^{-1} = n_h^{\mathrm{W,foil}}/r_{\mathrm{W,foil}} = 0.1936$ holes/eV. Finally, the number of holes for each Co-W sample can be calculated as $n_h^{\mathrm{W}} = C^{-1} r_{\mathrm{Co-W}}$.

Results for these calculations for both the Co-W alloy NPs and the bulk Co_3W alloy are listed in Table II. From these values we observe that the number of holes in W in the Co-W alloy NPs slightly increases with respect to that in metallic W, and to that found for the bulk Co_3W alloy, due to hybridization of the $5d$ band in W with the $3d$ band in Co. Moreover, we notice a further increase in n_h^{W} when the amount of Co in the sample increases, and when t_{W} decreases. This means that the electronic transfer from the $5d$ band in W to the $3d$ band in Co depends on the Co/W proportion in the samples. For the Co_3W alloy a slight increase in n_h^{W} with respect to the value of metallic W is also observed.

The ratio between the unoccupied states in the $5d_{5/2}$ and $5d_{3/2}$ bands in W, $n_h^{5/2}/n_h^{3/2}$, may be evaluated from the branching ratio I_{L3}/I_{L2}, following the analysis described in Ref. 24. The results of $n_h^{5/2}/n_h^{3/2}$ for the Co-W NPs and the bulk Co_3W alloy are given in Table II. Similar to n_h^{W}, we observe that this ratio varies depending on the Co/W proportion in the sample; i.e., $n_h^{5/2}/n_h^{3/2}$ increases when the Co/W ratio decreases, being highest for the bulk Co_3W alloy.

XMCD signals at the W $L_{2,3}$ on each sample were normalized according to factors obtained from XANES normalization. Figures 3(b) to 3(d) show XMCD signals for each Co-W NPs sample, and Fig. 4(b) for the Co_3W alloy. The XMCD integrals at L_3 and $L_{2,3}$ edges, defined as p and q, respectively, are also shown. The existence of a XMCD signal at W $L_{2,3}$ evidences the presence of an induced magnetic moment in the W atoms by the magnetic Co atoms in the Co-W alloy NPs and the Co_3W alloy. According to the direction of the applied magnetic field, and considering that the L_3 XMCD signal is mostly positive, while the L_2 XMCD is negative, we can determine that the induced W magnetic moment orients opposite to the direction of the field. Consequently, W induced moments are antiparallel to the Co magnetic moments deduced for the Co-W NPs in Ref. 9. This is consistent with the general trend in all transition metal series with the nd band filling: W has a less than half filled $5d$ band, which results in antiparallel coupling of its induced moment with that of the magnetic $3d$ metal.[10,14]

TABLE II. Values of x in the $Co_{1-x}W_x$ alloy, n_h^{W}, $n_h^{5/2}/n_h^{3/2}$ ratio, and $m_{\mathrm{L}}/m_{\mathrm{S}}$ ratio as calculated from the XMCD sum rules for the Co-W NPs samples in the present study and the bulk Co_3W alloy. $n_h^{\mathrm{W}} = 5.7$ holes for metallic W (Ref. 10).

Sample		x	n_h^{W}	$n_h^{5/2}/n_h^{3/2}$	$m_{\mathrm{L}}/m_{\mathrm{S}}$
Co-W NPs					
t_{Co} (nm)	t_{W} (nm)				
1.0	1.5	14.1(4)[a]	6.09(3)	0.50(1)	0.07(4)
0.7	0.6	18.2(4)[a]	6.06(5)	0.52(1)	0.13(5)
0.7	1.5	18.8(4)[a]	6.00(5)	0.54(1)	0.12(5)
Bulk Co_3W		25(1)	5.85(2)	0.59(1)	0.18(5)
Calc. Co_3W		25	5.96(2)	0.57(2)	0.10(2)

[a]Reference 9.

Values of p and q were used to calculate the orbital to spin moment ratio $m_{\mathrm{L}}/m_{\mathrm{S}}$ in the induced magnetic moments in W by applying the magneto-optical sum rules.[16,17] We have followed the symbol and sign criteria used in Ref. 25, so that the effective spin moment obtained from the sum rules is expressed as $m_{\mathrm{Seff}} = m_{\mathrm{S}} + m_{\mathrm{D}}$, where m_{D} represents the dipolar term, proportional to the expectation value of the magnetic dipole operator $\langle T_z \rangle$. Thus, in order to determine m_{S}, one has to consider the $\langle T_z \rangle$ value. For alloys with a noncubic structure, like the hcp Co_3W alloy, $\langle T_z \rangle$ might have a maximum value of $\langle S_z \rangle/3$, corresponding to the Lorentz local field at the W site, as described for Ir in Co-Ir alloys.[11] Following this approximation, $m_{\mathrm{Seff}} \leqslant 13/6\, m_{\mathrm{S}}$.

Notwithstanding, in the case of our amorphous Co-W alloy particles or in the polycrystalline Co_3W sample, where their individual anisotropy axes are randomly oriented, the angle averaged $\langle T_z \rangle$ becomes negligible, thus we consider below that $m_{\mathrm{S}} = m_{\mathrm{Seff}}$.[9] Moreover, we refrain from calculating absolute values of m_{S}, m_{L}, and m_{tot} in the Co-W NPs because of the uncertainty of the actual amount of W in their Co-W alloy, taking into account that not all of the W in the samples is alloyed with Co, as described in Sec. II.

$m_{\mathrm{L}}/m_{\mathrm{S}}$ results are listed in Table II. In all the Co-W systems in the present study $m_{\mathrm{L}}/m_{\mathrm{S}}$ in W is positive, which indicates that the orbital and spin moments in W are parallel aligned. Those values in the Co-W NPs samples are found to be nearly constant for a fixed amount of Co, and to decrease as the amount of Co in the sample increases. The latter may be understood as a reduction of the contribution of the orbital magnetism as the Co/W ratio in the sample increases. Comparing $m_{\mathrm{L}}/m_{\mathrm{S}}$ values for the Co-W NPs with that of the Co_3W alloy we observe that the latter is higher. This may also be related to the Co/W ratio on each alloy, as will be discussed in Sec. V.

For the Co_3W alloy, application of the sum rules yields to values of $m_S = -0.023(2)$, $m_L = -0.004(1)$, and $m_{tot} = -0.027(2)\ \mu_B$/W, for $n_h = 5.85$ holes in W atoms. The total magnetic moment in W for this alloy is one order of magnitude lower than the $-0.2\ \mu_B$/W moment measured for Fe/W multilayers in Ref. 10. However, the m_L/m_S ratio found in the Co_3W alloy is higher than in the experimental value reported for Fe/W multilayers,[10] but comparable to that estimated by first principles calculations for the latter system.[26]

IV. CALCULATIONS OF DOS, XANES AND XMCD

The electronic density of states (DOS) projected at the Co 3*d* and W 5*d* orbitals, as well as XANES and XMCD spectra at the Co *K* and the W $L_{2,3}$ edges in the Co_3W system have been calculated by using the *ab initio* code FDMNES.[27,28] This program gives the absorption cross section of photons around the ionization edge using fully relativistic monoelectronic calculations (DFT-LSDA). We have used the two different approaches for monoelectronic calculations that this code provides in order to simulate the x-ray absorption spectra: (i) a finite difference method to solve the Schrödinger equation, where the shape of the potential is free, thus a muffin-tin (MT) approximation can be avoided, and (ii) a Green formalism (multiple scattering) with a MT potential.

The structural and crystallographic information of the Co_3W system used to define the position of the absorbing and scattering atoms in the calculations is the one previously described in Sec. II. A cluster of 6 Å radius was used and a Fermi level of about 7701, 10199, and 11536 eV for the Co *K*, W L_3, and W L_2 edges, respectively. The initial parameters of the atomic electronic configurations of Co and W have been fixed as those obtained from the analysis of experimental XMCD (see W 5*d*-n_h^W in Table II). However, slightly modified electronic configurations were tested during the simulations in order to evaluate the dependence of the calculated XMCD signal with the initial moment in the Co and W n*d* bands, as will be described below.

A. DOS calculations

The spin polarized DOS projection at the Co 3*d* and W 5*d* orbitals for the Co_3W system were performed as described in Refs. 27 and 28, and are shown in Fig. 5. The traditional sign of hybridization[29] is observed on the curves; i.e., W 5*d* states follow the main features of the Co 3*d* DOS, specially in the energy region where the latter have their dominating weight.

The number of electrons in the W 5*d* band were calculated by integration of the DOS in Fig. 5, up to the Fermi energy E_f resulting in 4.04(2) electrons, or equivalently, 5.96(2) holes. This result is very close to the 5.85(2) holes calculated for the W 5*d* band from the W $L_{2,3}$ XANES analysis in Sec. III C. The difference between the number of electrons with spin up and down in the W 5*d* band amounts to 0.014(1) electrons, which results in an estimated spin magnetic moment of 0.014(1) μ_B. This value is on the same order of the m_S derived for the W atoms from the sum rules applied to the W $L_{2,3}$ XMCD results in the Co_3W alloy in Sec. III C. The difference between the two values may be an artifact of the calculation, due to the MT approximation on the form of the potential.[27]

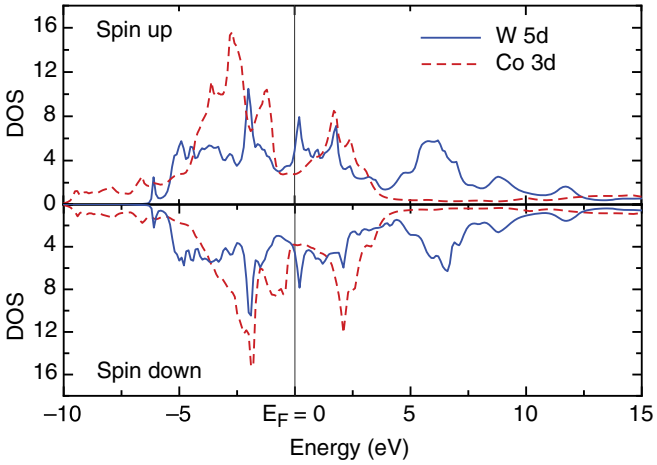

FIG. 5. (Color online) Calculated density of states (DOS) for the Co_3W system. DOS projected at the Co 3*d* (- -) and W 5*d* (–) orbitals. Spin-up DOS are shown as positive and spin-down as negative.

B. Co *K* edge

The calculated XMCD signal at the Co *K* edge for the Co_3W system is plotted in Fig. 6. A qualitative agreement between the simulated and the experimental curves for the Co_3W alloy is found both for XANES and XMCD.

The splitting of the negative peak observed in these Co-W systems at about 5 eV above the edge [marked as peak C in Fig. 2 and Fig. 6(b)] is reproduced in the calculations although the relative intensities and energy positions may vary. In particular, the energy positions of the calculated features above the edge are affected by inappropriateness of the description of the core-hole interaction in the monoelectronic framework

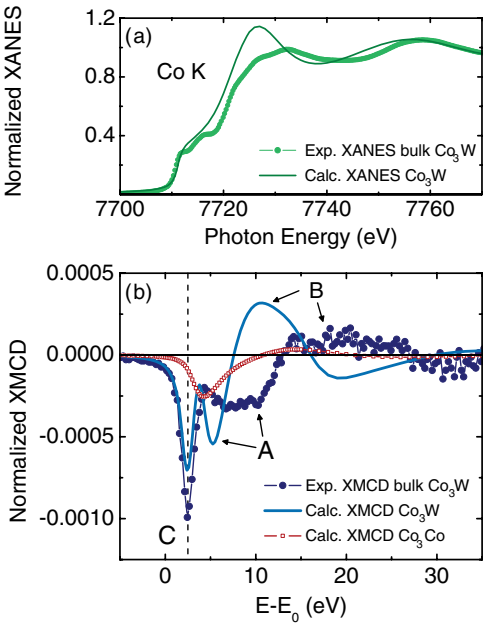

FIG. 6. (Color online) (a) Co *K* edge XANES spectra for the Co_3W system calculated with FDMNES (-) and comparison with the experimental one for the alloy (•). (b) Calculated Co *K* edge XMCD signal for a Co_3Co (□) and a Co_3W (-) system, and comparison with the experimental one for the Co_3W alloy (•).

of the finite-difference method calculation [peaks A and B in Fig. 6(b) are shifted to lower energies], and, therefore, the agreement with the experiment can only be expected to be qualitative. In order to take insight of the origin of the different peaks of the spectrum, we have calculated XAS and XMCD of a fictitious "Co_3Co" system with the Co_3W structure by substituting the W by Co in the definition of the cluster, and therefore eliminating the presence of 5*d* states in the calculation. The Co_3Co XMCD result is shown in Fig. 6 for comparison. Although the Co *K* edge XAS calculated in Co_3Co is only slightly different than Co_3W at the pre-edge feature, the Co_3Co XMCD is not split into two negative peaks, but closely resembles the bulk Co XMCD, which is similar to the measurement recorded in the Al_2O_3 capped Co NPs [see Fig. 2(a)]. The calculations confirm our conjecture (Sec. III B) on the origin of the splitting of the Co-*K* XMCD, and therefore, we positively ascribe the first negative XMCD peak experimentally observed in Co_3W to the hybridization of W 5*d* band states with the Co empty states probed in *K* edge absorption. Nominally, those are the Co 4*p* states through dipolar E1 transitions and the Co 3*d* states through quadrupolar E2 ones. However, the calculated Co *K* edge XMCD on Co_3W is split also when calculated in dipolar approximation only, showing that the hybridized W 5*d* band is probed also at the Co 4*p* states. Moreover, the correct sign of the calculated split XMCD feature [Fig. 6(b)] is only achieved for the (experimentally observed) antiparallel configuration between the Co magnetic moment and the W induced one, as is the general case for intermetallics with *less-than-half* and *more-than-half* filled bands.[30]

C. W $L_{2,3}$ edges

Calculations of the XANES and XMCD at the W $L_{2,3}$ edges were performed with the same FDMNES code. The intensity and spectral shape of the XMCD calculated signal is very sensitive to the Co magnetic moment introduced in the calculation. In contrast with the Co *K* edge, the spectral shape of the W XMCD is very sensitive to the approach used within the FDMNES code. In general, a rather satisfactory qualitative agreement is always found, achieving the best with the non-muffin-tin approximation, as shown in Fig. 7(a). The calculation confirms the antiparallel configuration between the Co magnetic moment and the W induced one, as described above. It is particularly interesting that the breakdown of the third Hund's rule for the W 5*d* magnetic moments in Co_3W ($m_L/m_S > 0$) is also described in the calculation, as shown in Fig. 7(b), where the experimental integrals are compared to the calculated ones. The signs of *p* and *q* are both positive, as in the experiments, leading to the same quantitative result (see values in Table II). Calculations with the multiple scattering formalism with a muffin-tin potential generate extra features which are not observed in the W $L_{2,3}$ XMCD.

V. DISCUSSION

The existence of a strong hybridization between the Co 4*p*−3*d* and W 5*d* orbitals in all the Co-W systems studied has been demonstrated both experimentally and theoretically. Our study of the W 5*d* band by XANES at the W $L_{2,3}$ edges and DOS calculations evidence electronic transfer from W

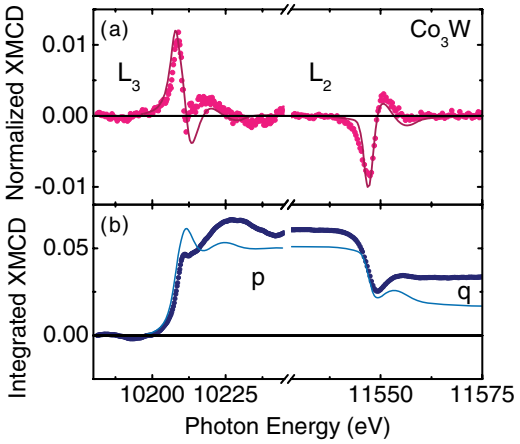

FIG. 7. (Color online) (a) Experimental (•) and calculated (–) XMCD signal at the $L_{2,3}$ edges of W in Co_3W. (b) Integrals of the experimental (•) and calculated (–) signals in (a).

5*d* through Co 4*p*−3*d* bands, and its dependence on the Co/W ratio in the samples. The main consequence of this hybridization is the existence of an induced magnetic moment in the W atoms in all the Co-W alloy systems. Moreover, the induced spin and orbital moments in W are found to be parallel aligned ($m_L/m_S > 0$), which is contrary to the prediction of Hund's third rule for W atoms since it is a less-than-half filled 5*d* band metal.

How hybridization may influence the breakdown of Hund's third rule in metallic compounds was originally proven by Galanakis *et al.* in a theoretical study on metallic VAu_4.[29] They nicely described how the spin-orbit (SO) in Au may influence the orbit in V atoms through hybridization, provoking the reversal of its orbital moment and, therefore, the breakdown of the mentioned rule. Subsequent works on metallic compounds make use of this interpretation to demonstrate that the strong hybridization between the different atoms in the magnetic compounds is the key factor of such a breakdown.[10,11,14] Similarly, in our Co-W alloy NPs and in the bulk Co_3W alloy, Co spin-orbit coupling can influence the induced W orbital moment causing its reversal.

The effect of the SO coupling in the reversal of the induced orbital moment in W in Fe/W multilayers is described by Wilhelm *et al.*[10] using a simple atomic picture based on the competition of interactions between the spin and orbital angular momentum projections in the 3*d* metal and W. Similarly, in our Co-W alloy systems, the interaction mechanisms may be examined as those then observed on Fe/W. The dominant interaction in all cases is the spin-spin interatomic exchange coupling between Co and W, $J_{inter} \cdot S_z^{Co} \cdot S_z^{W}$ which compels the spin in W to align antiparallel to Co. Then, there is a competition between the intra-atomic SO coupling in W, $\lambda_{intra} \cdot S_z^{W} \cdot L_z^{W}$, and the interatomic Co-W SO interaction $\lambda_{inter} \cdot S_z^{Co} \cdot L_z^{W}$. The breakdown of Hund's third rule occurs since the interatomic Co-W interaction overcomes the intra-atomic SO interaction in W, so that Co spin turns m_L^W to align antiparallel to m_S^{Co}, but parallel to m_S^W, resulting in $m_L/m_S > 0$ in W.

Further theoretical studies for the layered Fe/W system illustrate the influence of a large crystal field splitting in W, and the hybridization between Fe and W taking into account

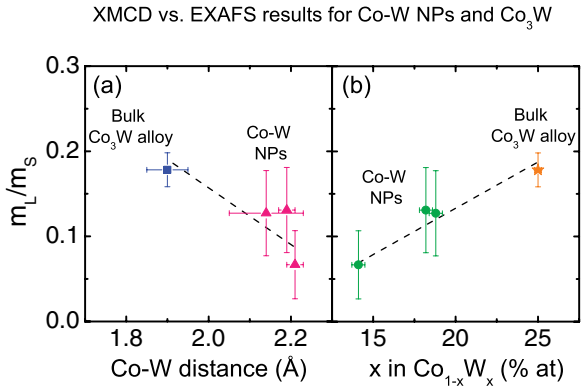

FIG. 8. (Color online) m_L/m_S ratio as calculated from the W $L_{2,3}$ XMCD signal for the Co-W alloy NPs and for the bulk Co_3W alloy, as a function of (a) the first Co-W interatomic distance obtained from EXAFS and (b) the composition of the Co-W alloy in the samples. Dashed lines: guide to the eye.

the band-filling and geometrical effects.[31–33] The latter are rather determinant, since the interatomic interactions between Fe and W are mediated by the crystal symmetry and interlayer distances; i.e., an increase of the interatomic Fe-W interaction is observed as the Fe and W interlayer distance decreases, which may be strongly related to the reversal of the orbital moment in W atoms.[31]

In fact, recent works on Fe-Zr and Co-Zr amorphous magnetic alloys discuss the strong relationship between the structural properties with the breakdown of Hund's third rule observed in these systems.[14] The dependence of Co(Fe) spin-orbit coupling with the reduction of the Co(Fe)-Zr interatomic distance and the coordination number is determined from first-principles calculations of the m_L/m_S ratio in Zr in the Co(Fe)-Zr alloys, as a function of the lattice parameter α for various crystallographic structures. A change in sign of m_L/m_S from negative to positive is observed as α decreases. Following an analogous analysis, we may correlate the structural results obtained on the Co-W alloy NPs[9] and on the bulk Co_3W alloy from EXAFS [Fig. 1] with the results of induced moments obtained by XMCD in the present work. In Fig. 8(a), the obtained m_L/m_S in W in all Co-W systems are plotted as a function of the first Co-W interatomic distance resulting from EXAFS analysis on the same samples. m_L/m_S is found to increase as the Co-W distance shortens. This trend agrees well with the one observed for calculated m_L/m_S versus α in Zr in the Co(Fe)-Zr alloys in Ref. 14. In the same study, Kapaklis *et al.* claim that the crystallinity of the materials is determinant in the breakdown of Hund's third rule since Zr induced moments in crystalline FeZrPt and CoZrPt alloys are found to fulfill the rule. In contrast, our observations of the breakdown of the rule on the polycrystalline bulk Co_3W, both experimentally and theoretically, demonstrate that the disorder level in the sample is not its main cause; instead, the reduction of the interatomic distances between dissimilar atoms seems to be the crucial point on this very controversial topic.

The Co influence on the orbital moment of W atoms in the samples may also be examined as a function of the Co/W in the alloy. In fact, m_L/m_S is found to scale with the W concentration in the Co-W alloy, as observed in Fig. 8(b). As was described in Sec. III C, this may be understood as an increase of the induced orbital component of the W magnetic moment as the Co/W proportion on the alloy decreases. A similar trend was observed for the m_L/m_S induced in Ir in Co-Ir disordered alloys, where Hund's third rule is also not fulfilled.[11]

Concluding, in all the Co-W alloy samples studied, i.e., Co-W alloy NPs and polycrystalline bulk Co_3W alloy, the induced W orbital moment orients parallel to its spin moment, contrary to the prediction of Hund's third rule for W. This breakdown has been proven by experimental and simulated XANES spectra and XMCD signals at the Co K and W $L_{2,3}$ edges. Consequently, we demonstrate that W not only affects the local structure of Co NPs, but also their electronic structure. The Co $3d-$W $5d$ hybridization is evidenced and becomes a key factor in the breakdown of this rule in the case of induced moments. Our comparison between XMCD and EXAFS results demonstrate that the influence of the Co-W spin-orbit coupling depends on the average Co-W interatomic distance, as a consequence of the dependence of the strength of the hybridization. Contrary to the differences found for crystalline and amorphous Co(Fe)-Zr alloys in Ref. 14, we observe the breakdown of Hund's third rule in both amorphous and polycrystalline Co-W systems, which suggests that this behavior is not a general one, but it depends on the studied material and its local structure. In the case of W systems, our work suggests that the breakdown of this rule is a rather general trend, taking place not only in metallic thin films, but also in nanoparticulate and bulk materials.

ACKNOWLEDGMENTS

The financial support of the Spanish MINECO MAT2011-23791 and Aragonese DGA-IMANA (co-funded by the European Social Fund) projects is acknowledged. A.I.F. acknowledges a CSIC JAE2008-Predoc grant. ESRF beamtime corresponds to HE2238, HE2541, and HE2952 experiments. We thank the support of S. Pascarelli during the EXAFS experiment, as well as fruitful discussions with O. Bunău regarding the FDMNES calculations.

*figueroa@unizar.es

[1] J. Bansmann, S. H. Baker, C. Binns, J. A. Blackman, J. P. Bucher, J. D. Dávila, V. Dupuis, L. Favre, D. Kechrako, A. Kleibert, K. H. Meiwes-Broer, G. M. Pastor, A. Perez, O. Toulemonde, K. N. Trohidou, J. Tuaillon, and Y. Xie, Surf. Sci. Rep. **56**, 189 (2005).

[2] N. A. Frey, S. Peng, K. Cheng, and S. Sun, Chem. Soc. Rev. **38**, 2532 (2009).

[3] C. Antoniak, J. Lindner, M. Spasova, D. Sudfeld, M. Acet, M. Farle, K. Fauth, U. Wiedwald, H.-G. Boyen, P. Ziemann, F. Wilhelm, A. Rogalev, and S. Sun, Phys. Rev. Lett. **97**, 117201 (2006).

[4] J. Bartolomé, L. M. García, F. Bartolomé, F. Luis, R. López-Ruiz, F. Petroff, C. Deranlot, F. Wilhelm, A. Rogalev, P. Bencok, N. B. Brookes, L. Ruiz, and J. M. González-Calbet, Phys. Rev. B **77**, 184420 (2008).

[5]A. Fraile Rodríguez, A. Kleibert, J. Bansmann, A. Voitkans, L. J. Heyderman, and F. Nolting, Phys. Rev. Lett. **104**, 127201 (2010).
[6]C. Antoniak, A. Warland, M. Darbandi, M. Spasova, A. Trunova, K. Fauth, E. F. Aziz, M. Farle, and H. Wende, J. Phys. D. Appl. Phys. **43**, 474007 (2010).
[7]F. Jiménez-Villacorta, C. Prieto, Y. Huttel, N. D. Telling, and G. van der Laan, Phys. Rev. B **84**, 172404 (2011).
[8]M. Niemeyer, K. Hirsch, V. Zamudio-Bayer, A. Langenberg, M. Vogel, M. Kossick, C. Ebrecht, K. Egashira, A. Terasaki, T. Möller, B. v. Issendorff, and J. T. Lau, Phys. Rev. Lett. **108**, 057201 (2012).
[9]A. I. Figueroa, J. Bartolomé, L. M. García, F. Bartolomé, C. Magén, A. Ibarra, L. Ruiz, J. M. González-Calbet, F. Petroff, C. Deranlot, S. Pascarelli, P. Bencok, N. B. Brookes, F. Wilhelm, and A. Rogalev, Phys. Rev. B **84**, 184423 (2011).
[10]F. Wilhelm, P. Poulopoulos, H. Wende, A. Scherz, K. Baberschke, M. Angelakeris, N. K. Flevaris, and A. Rogalev, Phys. Rev. Lett. **87**, 207202 (2001).
[11]V. V. Krishnamurthy, D. J. Singh, N. Kawamura, M. Suzuki, and T. Ishikawa, Phys. Rev. B **74**, 064411 (2006).
[12]F. Hund, Z. Phys. **33**, 345 (1925).
[13]J. Herrero-Albillos, L. M. García, F. Bartolomé, and A. T. Young, Europhys. Lett. **93**, 17006 (2011).
[14]V. Kapaklis, P. T. Korelis, B. Hjörvarsson, A. Vlachos, I. Galanakis, P. Poulopoulos, K. Özdoğan, M. Angelakeris, F. Wilhelm, and A. Rogalev, Phys. Rev. B **84**, 024411 (2011).
[15]Y. H. Matsuda, J. L. Her, S. Michimura, T. Inami, M. Suzuki, N. Kawamura, M. Mizumaki, K. Kindo, J. Yamauara, and Z. Hiroi, Phys. Rev. B **84**, 174431 (2011).
[16]B. T. Thole, P. Carra, F. Sette, and G. vanderLaan, Phys. Rev. Lett. **68**, 1943 (1992).
[17]P. Carra, B. T. Thole, M. Altarelli, and X. Wang, Phys. Rev. Lett. **70**, 694 (1993).
[18]J. Rodriguez-Carvajal, Phys. Rev. B **192**, 55 (1993).
[19]http://icsd.iqfr.csic.es/icsd/
[20]F. Wilhelm, N. Jaouen, A. Rogalev, W. G. Stirling, R. Springell, S. W. Zochowski, A. M. Beesley, S. D. Brown, M. F. Thomas, G. H. Lander, S. Langridge, R. C. C. Ward, and M. R. Wells, Phys. Rev. B **76**, 024425 (2007).
[21]J. P. Rueff, R. M. Galéra, C. Giorgetti, E. Dartyge, C. Brouder, and M. Alouani, Phys. Rev. B **58**, 12271 (1998).
[22]S. Pizzini, A. Fontaine, C. Giorgetti, E. Dartyge, J.-F. Bobo, M. Piecuch, and F. Baudelet, Phys. Rev. Lett. **74**, 1470 (1995).
[23]B. L. Henke, E. M. Gullikson, and J. C. Davis, At. Data Nucl. Data Tables **54**, 181 (1993).
[24]A. N. Mansour, J. J. W. Cook, and D. E. Sayers, J. Phys. Chem. **88**, 2330 (1984).
[25]J. Stohr, J. Electron Spectrosc. Relat. Phenom. **75**, 253 (1995).
[26]I. Galanakis, M. Alouani, and H. Dreyssé, Phys. Rev. B **62**, 3923 (2000).
[27]Y. Joly, Phys. Rev. B **63**, 125120 (2001).
[28]O. Bunău and Y. Joly, J. Phys.: Condens. Matter **21**, 345501 (2009).
[29]I. Galanakis, P. M. Oppeneer, P. Ravindran, L. Nordström, P. James, M. Alouani, H. Dreysse, and O. Eriksson, Phys. Rev. B **63**, 172405 (2001).
[30]I. A. Campbell, J. Phys. F **2**, L47 (1972).
[31]X. Qian and W. Hübner, Phys. Rev. B **67**, 184414 (2003).
[32]R. Tyer, G. van der Laan, W. M. Temmerman, Z. Szotek, and H. Ebert, Phys. Rev. B **67**, 104409 (2003).
[33]H. Wende, Rep. Prog. Phys. **67**, 2105 (2004).